energies

MDPI

Article

Single-Loop Triple-Diameter Pulsating Heat Pipes at Reduced Heat Input: A CFD Study on Inner Diameter Optimization

Rasoul Fallahzadeh, Masoud Hatami Garousi, Luca Pagliarini, Fabio Bozzoli and Luca Cattani *

Department of Engineering for Industrial Systems and Technologies, University of Parma, 43124 Parma, Italy; fabio.bozzoli@unipr.it (F.B.)

* Correspondence: luca.cattani1@unipr.it

Abstract: The geometric configuration, particularly the inner tube diameter, plays a significant role in the thermal performance of pulsating heat pipes (PHPs). Previous experimental research has demonstrated that single-loop triple-diameter PHPs (TD-PHPs) outperform single-loop single-diameter PHPs (SD-PHPs) and dual-diameter PHPs (DD-PHPs) in terms of thermal performance under moderate heating input powers ranging from 25 W to 75 W. However, a reduction in heat input from 75 W to 25 W leads to a diminished impact of TD-PHPs on the thermal performance. Therefore, to improve the overall performance of TD-PHPs, this study used two-dimensional transient computational fluid dynamics simulations to identify the optimal inner tube diameters for TD-PHPs at a low heat input by evaluating the thermal resistance of five TD-PHPs with various inner diameters. The findings reveal that the TD-PHP configuration exhibits minimum thermal resistance, with inner diameters of 4.5 mm for the upper arch (the condenser section), 4.0 mm for the wide branch, and 2.5 mm for the narrow branch, primarily due to its full circulation flow pattern. Furthermore, the overall heat transfer performance of the optimal TD-PHP was compared with that of an SD-PHP at low heat inputs (10 and 18 W), indicating that although the optimal TD-PHP shows lower thermal resistance, it does not significantly affect the start-up time.

Keywords: triple-diameter pulsating heat pipe; numerical simulation; diameter optimization; flow pattern; thermal resistance

check for updates

Citation: Fallahzadeh, R.; Garousi, M.H.; Pagliarini, L.; Bozzoli, F.; Cattani, L. Single-Loop Triple-Diameter Pulsating Heat Pipes at Reduced Heat Input: A CFD Study on Inner Diameter Optimization. *Energies* **2024**, *17*, 5568. https://doi.org/10.3390/en17225568

Academic Editor: Frede Blaabjerg

Received: 20 September 2024
Revised: 30 October 2024
Accepted: 5 November 2024
Published: 7 November 2024

Copyright: © 2024 by the authors. Licensee MDPI, Basel, Switzerland. This article is an open access article distributed under the terms and conditions of the Creative Commons Attribution (CC BY) license (https://creativecommons.org/licenses/by/4.0/).

1. Introduction

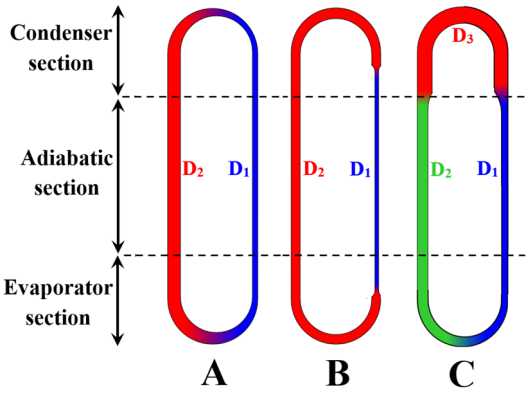
Due to the progressive and fast miniaturization of electronic components, the heat flux densities to be effectively dissipated have substantially increased [1]. This represents a critical aspect of chip integrity and thermal failure prevention. Typical thermal management solutions are based on active heat transfer and cooling systems, which require substantial electrical energy [2]. Although these pieces of equipment have high reliability and control capabilities, passive thermal management techniques represent a viable and cost-effective alternative. Researchers have specifically focused on studying and developing two-phase passive heat transfer devices, which offer superior heat dissipation performance compared with single-phase systems because of their latent heat contribution [3]. The two-phase passive heat transfer field has historically employed thermosyphons (wickless) and heat pipes (wicked). Pulsating (called also oscillating) heat pipes (PHPs), first patented by Akachi in the early 1990s [4], are the most recent evolution of wickless devices, which could have excellent potential for many industrial applications [5]. PHPs, in their most straightforward layout, consist of a capillary tube partially filled with a working fluid and bent between two areas, namely the evaporator section, where the external environment provides heat, and the condenser section, where the heat is dissipated. In the evaporator section, the supplied heat results in a local increase in temperature; the unbalanced temperature between the evaporator and the condenser sections leads to an unbalanced internal pressure, which acts as the driving force for the working fluid through a transport section named the adiabatic section.

Several factors substantially affect the thermal transfer efficiency of PHPs, including the geometry, selected working fluid, filling ratio (FR = working fluid volume/total PHP volume), and orientation [6–8]. Regarding the geometric characteristics, researchers have identified various features that influence the overall operation, including the length of the evaporator/condenser, the inner/outer diameter of the tube, and the number of turns [9]. The latter is essential in promoting and stabilizing fluid flow at various inclination angles, thereby improving heat transfer performance. A higher number of turns usually ensures improved internal pressure disturbance and orientation-independent functioning [10,11]. However, adjacent channels interacting with each other regarding heat exchange, pressure instabilities, and phase change dramatically increase the complexity of the PHP's underlying physics. As stressed by Nikolayev [12] and Pagliarini et al. [13] in their review works, this yields a hard conceptualization of predictive tools for the PHP operation, thus undermining the reliability of such devices for large-scale industrial employment. As a result, single-loop PHPs may represent an exciting and effective thermal management alternative to multi-turn PHPs. The much lower overall complexity could ensure a higher predictability than classical multi-turn PHPs. Moreover, the thermal performance of single-loop PHPs working in parallel may be comparable with (if not superior to) that of equivalent multi-turn PHPs having the same number of branches [14], especially in a bottom-heating mode (i.e., the evaporator section is placed below the condenser section). Single-loop PHP thermal performance optimization is thus crucial to achieving competitive heat transfer solutions concerning the available two-phase passive systems.

Considering single-loop PHPs, other researchers have proposed optimization attempts through novel geometrical arrangements. Sedighi et al. [15] proposed an additional branch in the evaporator section acting as a secondary bubble pump. The new configuration was experimentally tested and compared with the conventional single-loop PHP. The modified geometry exhibited lower and more stable temperature fluctuations, and the overall thermal response was better than that of the conventional layout for low and high FRs. Moreover, the additional branch provided a more orientation-independent operation. Similar modified layouts were numerically studied by Kommuri et al. [16], who reported improved start-up times from 22.4% up to 32.6%. The additional branch pro-moted stable, unidirectional flow, producing approximately 16% higher fluid flow velocities. Such enhanced performances resulted from improved local heat transfer in the evaporator section by minimizing the saturation temperature. Using a two-dimensional numerical model, Kang et al. [17] investigated single-loop PHPs with separate walls within the flow channel. Heat transfer efficiency at low FRs ($\leq$50%) was enhanced by positioning the dividing wall closer to the inner side of the single-loop PHP channel. The dividing wall at the center of the channel exhibited minimal thermal resistance at an FR of 70%. However, conventional techniques may struggle to produce single-loop PHPs with dividing walls.

Another viable option for heat transfer augmentation through modified geometrical features is represented by asymmetric layouts, such as branches that have an uneven inner diameter, which increase the probability of annular and circulatory flows being sustained in preferential directions. One of the first works to suggest such a layout alteration was by Liu et al. [18] for multi-turn PHPs, which motivated many subsequent studies (see Refs. [19–28], for example). Therefore, researchers proposed similar asymmetric configurations for single-loop PHPs, known as single-loop dual-diameter PHPs (DD-PHPs), with layouts presenting two different inner diameters, or single-loop triple-diameter PHPs (TD-PHPs), with layouts presenting three different inner diameters. Table 1 summarizes previous works that investigated and optimized single-loop DD-PHPs and TD-PHPs.

Table 1. Summary of studies focused on single-loop DD-PHP and TD-PHP configurations.



Author(s)	Research Method	Configuration Type	Key Findings
Kwon and Kim [29]	Experimental study	A	• Compared with the SD-PHP, the DD-PHPs enhance the circulation of the working fluid, thereby reducing thermal resistance and diminishing its dependence on the inclination angle. • An optimal range of diameter differences exists for the DD-PHPs that maximizes thermal performance enhancement.
Kwon and Kim [30]	Experimental study	A	• Developing a simple model to predict the thermal resistance of the DD-PHPs. • An optimal range of diameter differences exists for the DD-PHPs that maximizes thermal performance enhancement.
Wang et al. [31]	Numerical simulation	B	• Under identical heat input conditions, the SD-PHP and DD-PHPs exhibit distinct start-up behaviors. • An optimal range of diameter differences exists for the DD-PHPs that maximizes thermal performance enhancement.
Fallahzadeh et al. [32]	Experimental study	A and C	• The TD-PHP demonstrates lower thermal resistance at a 90° inclination angle than the SD-PHP and DD-PHP at medium heat input power (25–75 W). • In contrast to the SD-PHPs, at a 90° inclination angle, the DD-PHPs' and TD-PHPs' thermal resistance is relatively insensitive to changes in the FR.
Liu et al. [33]	Numerical simulation	A	• The thermal performance of the DD-HPs is less sensitive to changes in the inclination angles compared with the SD-PHP. • Compared with the SD-PHP, the DD-PHPs exhibit reductions in the start-up time and thermal resistance. • The optimal FR for the DD-PHPs varies according to the heating input power.

These studies revealed that DD-PHPs and TD-PHPs generally achieve higher thermal efficiency than SD-PHPs. On the one hand, research shows that modifying the inner diameter ratios of DD-PHPs can significantly enhance their thermal performance by optimizing the heat transfer capabilities [29–31]. On the other hand, TD-PHPs consistently outperform DD-PHPs, suggesting a more significant potential for their application in systems requiring high thermal efficiency [32]. Moreover, the thermal performance of DD-PHPs and TD-PHPs is more sensitive to changes in the heating input power than to adjustments in the inclination angles [32,33] and FRs [32]. Although, even at low heat inputs, DD-PHPs and TD-PHPs showed better thermal performance than SD-PHPs [30,32], their thermal resistance is not very satisfactory. For example, our previous experimental study [32] demonstrated that a reduction in heat input from 75 W to 25 W resulted in a diminished influence of TD-PHPs on thermal performance. Therefore, enhancement of TD-PHP thermal performance at

lower heat inputs (<25 W) is necessary to augment their overall effectiveness, which is also critical in certain PHP applications, such as batteries' thermal management systems [34]. Therefore, this study investigated various inner diameters of TD-PHPs to determine the optimal configuration for efficient operation under conditions of reduced heat input power.

This paper's structure is as follows. Section 2 covers the models and methodologies, including descriptions of the geometric model, boundary conditions, and mathematical model. Section 3 examines how different inner tube diameters affect the thermal resistance of TD-PHPs at a low heat input (18 W), identifies the optimal diameters, and then compares the performance of the obtained optimal TD-PHP with that of an SD-PHP at two low heat inputs (10 and 18 W). Section 4 finally delineates the investigation's results.

2. Models and Methodologies

2.1. Geometric Model Description

This investigation assessed the influence of varying inner tube widths on the efficacy of TD-PHPs via the analysis of two-dimensional PHPs. Figure 1 illustrates that the lengths of the evaporator, adiabatic, and condenser sections were set at 60 mm, 60 mm, and 30 mm. The division between the two branches was set at 20 mm. The geometric parameters utilized in this study were selected on the basis of experimental work conducted by Saha et al. [35]. This approach allows for the verification of the simulation results against the experimental data, as will be discussed in detail in Section 3.1. Moreover, PHPs were partially filled with water as the working fluid at an FR of 50%, which Saha et al. [35] identified as the optimum FR. To streamline the computational modeling, the walls of the PHPs were omitted, focusing solely on simulating the working fluid. All PHPs were analyzed in a bottom-heating mode, corresponding to an inclination angle of 90°. Two distinct configurations of single-loop PHPs were designed, as depicted in Figure 1.

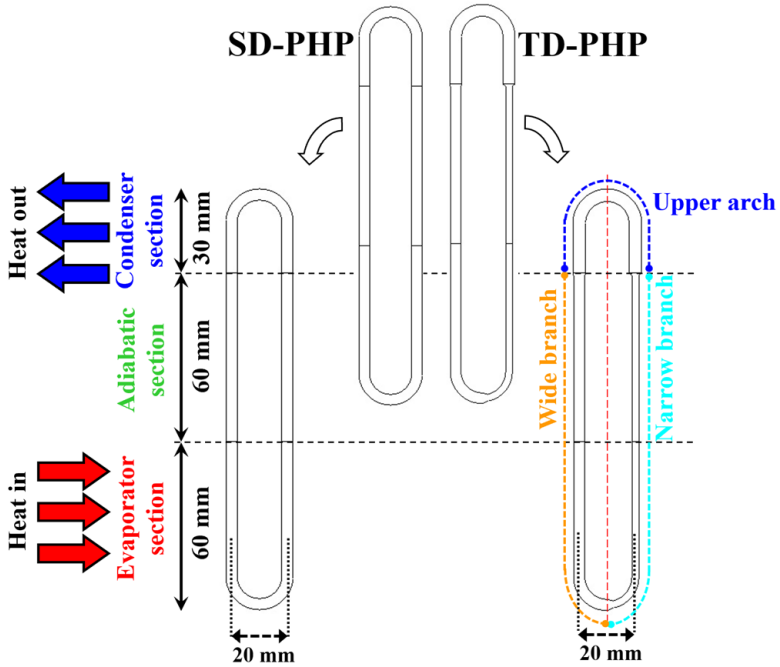


Figure 1. Schematic representations of the simulated SD-PHP and TD-PHP.

The first configuration, referred to as the symmetrical and uniform diameter single-loop PHP (SD-PHP), featured a uniform inner diameter and serves as a baseline for comparative thermal performance studies with the second configuration, the TD-PHP. The TD-PHPs were derived from the SD-PHP by altering the inner diameters of the upper arch (condenser section) and the wide and narrow branches.

The ratio of buoyant force to surface tension force significantly affects the formation of flow patterns in PHPs. A significantly small inner tube diameter (ID) increases the flow resistance, resulting in reduced heat transfer efficiency, while an excessively large ID reduces the influence of surface tension and prevents the PHP from functioning properly. Therefore, identifying the maximum and minimum critical ID values is essential to ensure the effective functioning of PHPs. The recommended range for ID is suggested to be as follows [8]

$$0.7\sqrt{\frac{\sigma}{(\rho_l-\rho_v)g}} \leq \mathrm{ID} < 2\sqrt{\frac{\sigma}{(\rho_l-\rho_v)g}} \quad (1)$$

where σ represents the surface tension, ρ_l denotes the liquid density, ρ_v indicates the vapor density, and g is the gravitational acceleration. By utilizing Equation (1), the maximum and minimum critical ID values for PHPs with water as the working fluid are illustrated as a function of temperature in Figure 2. It is evident that with increased temperature, both the maximum and minimum critical diameters slightly decrease. Nevertheless, the minimum value of the maximum critical ID is 5.007 mm, while the maximum value of the minimum critical ID is 1.908 mm.

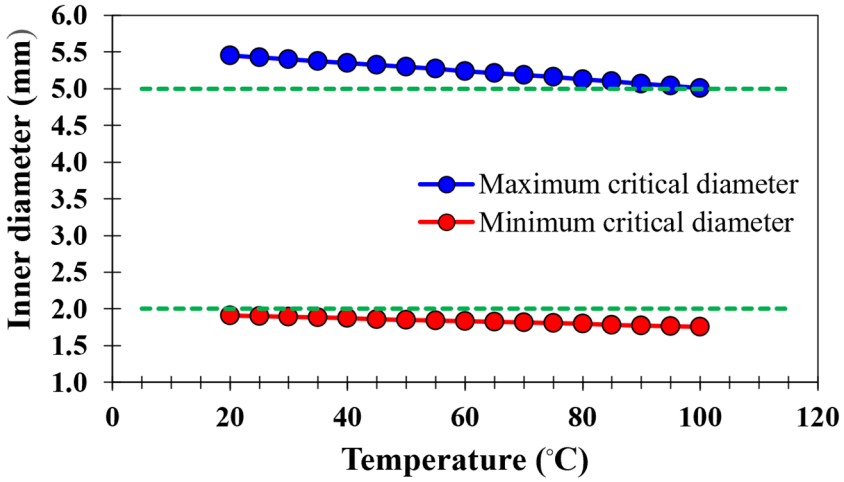


Figure 2. Dependence of the maximum and minimum critical IDs on temperature (considering water as the working fluid).

Therefore, this study selected six single-loop PHPs—one SD-PHP and five TD-PHPs—with IDs between 2 and 5 mm, as detailed in Table 2.

Table 2. The selected IDs for the simulated single-loop PHPs.

Single-Loop PHP Configuration	PHP No.	ID (mm)		
		Wide Branch	Narrow Branch	Upper Arch
SD-PHP	SD-PHP	4	4	4
TD-PHP	TD-PHP1	4	3.5	4.5
	TD-PHP2	4	3	4.5
	TD-PHP3	4	2.5	4.5
	TD-PHP4	4	2	4.5
	TD-PHP5	4	2.5	5

A two-dimensional structured quadrilateral mesh for the PHPs was created. Figure 3 provides an illustrative example of this mesh applied to TD-PHP3.

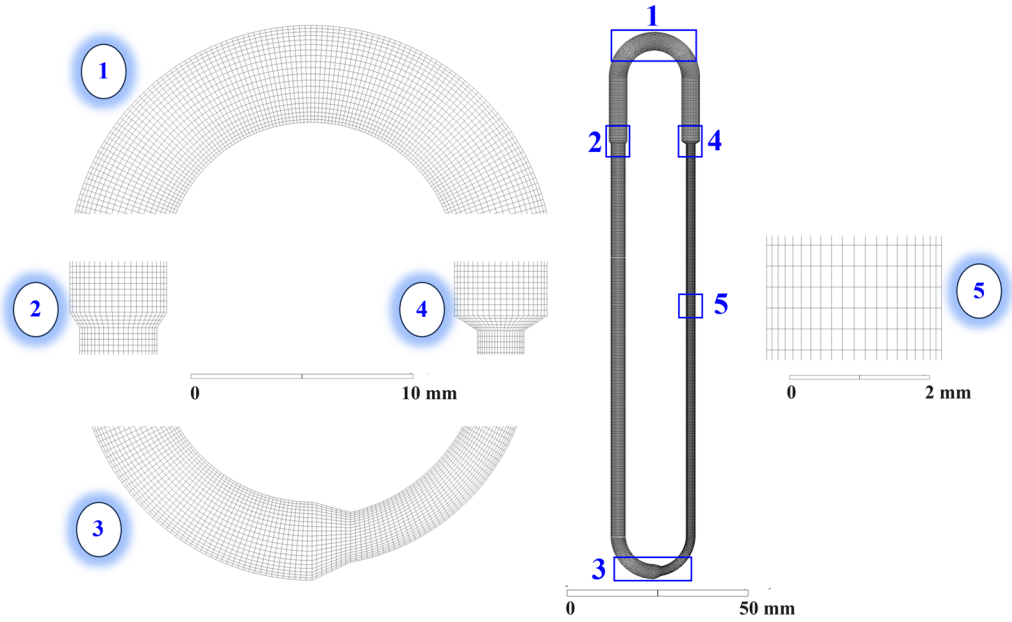


Figure 3. Meshing configuration of the computational domain for TD-PHP3.

2.2. Description of the Boundary Conditions

In all simulations, the condenser component was maintained at a constant temperature of 298.15 K (25 °C), whereas the adiabatic portion underwent a heat flow of 0 W/m^2. A steady heat transfer (q) was imposed on the boundary condition of the two-dimensional evaporator section, which may be determined using the following expression

$$q = \frac{Q}{A_{evp}} \tag{2}$$

where Q signifies the heating input power and A_{evp} denotes the heating area of the evaporator section.

2.3. Description of the Mathematical Model

Numerical simulations were conducted using ANSYS Fluent (2024 R1), which has demonstrated its reliability in performing CFD simulations of fluid flow and heat transfer across various applications, including tube heat exchangers [36], thermosyphons [37], and PHPs [17]. The present numerical simulation employed the VOF multiphase flow model to monitor the boundary between the liquid water and vapor phases by computing the volume fraction (α) of each phase inside each computational cell. In this configuration, liquid water is identified as the primary phase, whereas vapor water is categorized as the secondary phase. The VOF formulation operates on the principle that the two phases do not interpenetrate; consequently, each computing cell is occupied by either one phase or a combination of both. The phases demonstrate shared fields for all variables and characteristics, suggesting volume-averaged values, provided that each phase's volume fraction is identified at each location. The variables and characteristics inside each cell indicate either a singular phase or a composite of phases, relying on the volume fraction α_l and α_v, where the subscripts l and v denote liquid and vapor, correspondingly. When $\alpha_v = 1$, the computational cell is entirely occupied by the vapor phase; when $\alpha_v = 0$, the computational cell is entirely occupied by the liquid phase; and when $0 < \alpha_v < 1$, the computational cell contains a mixture of vapor and liquid phases. Furthermore, for each control volume, the volume fractions of the liquid and vapor phases sum to unity, as described in Equation (3):

$$\alpha_l + \alpha_v = 1 \tag{3}$$

The geometric reconstruction method was used to capture the vapor–liquid interface. The following paragraphs elaborate on the governing equations for mass continuity, momentum, and energy in the VOF model [38].

For vapor and liquid phases, the mass continuity equations are expressed as

$$\frac{\partial \alpha_l}{\partial t} + \nabla\left(\alpha_l \vec{v}\right) = \frac{S_{m,l}}{\rho_l} \tag{4}$$

$$\frac{\partial \alpha_v}{\partial t} + \nabla\left(\alpha_v \vec{v}\right) = \frac{S_{m,v}}{\rho_v} \tag{5}$$

where $\vec{v}$ denotes the velocity of the working fluid, and ρ_l and ρ_v are the density of the liquid and vapor phases, respectively. $S_{m,l}$ and $S_{m,v}$ are the source terms of the mass transfer of the liquid and vapor phases, used to illustrate the processes of evaporation and condensation, which are delineated in the following [39]

$$S_{m,l} = \begin{cases} -\beta_1 \alpha_l \rho_l \left|\frac{T-T_{sat}}{T_{sat}}\right| & (\text{Evaporation process} : T \geq T_{sat}) \\ \beta_2 \alpha_v \rho_v \left|\frac{T-T_{sat}}{T_{sat}}\right| & (\text{Condensation process} : T < T_{sat}) \end{cases} \tag{6}$$

$$S_{m,l} = \begin{cases} \beta_1 \alpha_l \rho_l \left|\frac{T-T_{sat}}{T_{sat}}\right| & (\text{Evaporation process} : T \geq T_{sat}) \\ -\beta_2 \alpha_v \rho_v \left|\frac{T-T_{sat}}{T_{sat}}\right| & (\text{Condensation process} : T < T_{sat}) \end{cases} \tag{7}$$

where T_{sat} is the saturation temperature, which is dependent on the local pressure (p) [17]:

$$T_{sat} = \frac{237.3 \ln\left(\frac{p}{610.78}\right)}{17.27 - \ln\left(\frac{p}{610.78}\right)} + 273.15 \tag{8}$$

Furthermore, in Equations (6) and (7), the parameters β_1 and β_2 represent time relaxation factors that significantly influence the evaporation and condensation processes. A low relaxation coefficient may lead to a deviation of the temperature at the liquid-vapor interface from the saturation temperature, thereby diminishing the accuracy of the numerical simulation. On the other hand, a high relaxation coefficient can create challenges in achieving convergence of the governing equations. These empirical coefficients for vaporization and condensation, denoted as β_1 and β_2 respectively, are primarily influenced by the type of working fluid and the operating conditions. These coefficients can vary considerably depending on the specific circumstances. For this study, the values of β_1 and β_2 are fixed at 0.1 and 6 s^{-1}, respectively [17].

The momentum equation in the VOF model is expressed as follows:

$$\frac{\partial}{\partial t}\left(\rho \vec{v}\right) + \nabla\left(\rho \vec{v} \vec{v}\right) = -\nabla p + \nabla\left[\mu\left(\nabla \vec{v} + \nabla \vec{v}^{T}\right)\right] + \rho \vec{g} + \vec{F} \tag{9}$$

Accordingly, ρ and μ denote the volume-averaged density and volume-averaged dynamic viscosity. Their computations are as follows:

$$\rho = \alpha_l \rho_l + \alpha_v \rho_v \tag{10}$$

$$\mu = \alpha_l \mu_l + \alpha_v \mu_v \tag{11}$$

In addition, $\vec{F}$ denotes the momentum source term characterized by body forces. It originates from the continuous surface force model proposed by Brackbill et al. [40]. Given that just vapor and liquid are present in the operating process, the simplified calculation technique is as follows

$$\vec{F} = \sigma_{lv} \frac{\rho k_l \nabla \alpha_l}{\frac{1}{2}(\rho_l + \rho_v)} \tag{12}$$

where σ_{lv} indicates the surface tension coefficient between the liquid and vapor phases, and k_l symbolizes the liquid meniscus, whereas $\nabla\alpha_l$ depicts the gradient of the liquid volume fraction, demonstrating the normal direction of the interface. Assuming that n is the interface normal ($n = \nabla\alpha_l$), Equation (13) illustrates that the curvature k_l is equal to the divergence of the unit normal:

$$k_l = \nabla.\frac{n}{|n|} = \frac{\nabla\alpha_l}{|\nabla\alpha_l|} \tag{13}$$

The energy equation, which is illustrated below, is shared by the liquid and vapor phases, much as the momentum equation:

$$\frac{\partial}{\partial t}(\rho E) + \nabla\cdot\left(\vec{v}(\rho E+\rho)\right) = \nabla\cdot(k_{eff}\nabla T) + S_h \tag{14}$$

The energy transfer due to conduction is represented by $\nabla\cdot(k_{eff}\nabla T)$, and the effective thermal conductivity is displayed by k_{eff}

$$k_{eff} = k + k_t \tag{15}$$

where k_t denotes the turbulent thermal conductivity as explained by the turbulent model, and k indicates the volume-averaged effective thermal conductivity, calculated as follows:

$$k = \alpha_l k_l + \alpha_v k_v \tag{16}$$

In Equation (14), E denotes the internal energy, computed employing volume averaging, as demonstrated in Equation (17)

$$E = \frac{\alpha_l\rho_l C_{p,l}(T - T_{sat}) + \alpha_v\rho_v C_{p,v}(T - T_{sat})}{\alpha_l\rho_l + \alpha_v\rho_v} \tag{17}$$

where $C_{p,l}$ and $C_{p,v}$ represent the specific heat of liquid and vapor phases, respectively. Moreover, in Equation (14), S_h represents the latent heat of the phase transition

$$S_h = h_{LH}S_{m,l} = -h_{LH}S_{m,v} \tag{18}$$

where h_{LH} signifies the latent heat of vaporization, which is calculated as [41]:

$$h_{LH} = \left(2.5 \times 10^6\right) - \left(2.386 \times 10^3(T_{sat} - 273)\right) \tag{19}$$

In addition, the following assumptions were adopted in all simulation cases.

1. The contact angle of liquid water on the tube walls was determined to be 30° [42].
2. The density and viscosity of the liquid water were defined as temperature functions and given by [17]:

$$\rho_l = \begin{bmatrix} 999.83952 + (16.94517T) - \left(7.9870401 \times 10^{-3}T^2\right) - \left(46.170461 \times 10^{-6}T^3\right) \\ + \left(105.56302 \times 10^{-9}T^4\right) - \left(280.54253 \times 10^{-12}T^5\right) \end{bmatrix} / \left[1 + 16.87985 \times 10^{-3}T\right] \tag{20}$$

$$\mu_l = 1.856 \times 10^{-14}\exp\left(\left(\frac{4209}{T}\right) + (0.04527T) - \left(3.376 \times 10^{-5}T^2\right)\right) \tag{21}$$

Note that T in Equation (20) is in degrees Celsius.

3. The vapor phase was assumed to be compressible. To obtain pressure field distribution, the vapor phase was considered an ideal gas, and thus the ρ_v was calculated by:

$$\rho_v = \frac{p}{R_g T} \tag{22}$$

R_g specifies the specific gas constant of vapor, equal to 461.52 J/(kg·K). It is important to acknowledge that a constant value of 1.34×10^5 Pa·s was applied for μ_v.

4. The friction between vapor plugs and tube walls was negligible.
5. A constant value of 0.072 N/m [17] was set to calculate the interfacial tension between the liquid and vapor phases (σ_{lv}).

3. Results and Discussion

3.1. Validation of Numerical Method

After conducting numerous simulations using varying time steps (from 10^{-5} to 10^{-3} s), a value of 10^{-5} s was determined to be optimal. This implies that smaller time steps were found to be computationally expensive without a significant improvement in accuracy, while larger time steps resulted in unstable solutions, failing to converge to the correct answer. Prior to validating the numerical method, a mesh independence verification was performed using four different mesh densities. The results, as shown in Table 3, demonstrate that the thermal resistance values converge and remain nearly constant when the mesh density exceeds 16,200 elements. Therefore, a mesh density of 16,200 elements was selected for the subsequent numerical simulations to ensure both accuracy and computational efficiency.

Table 3. Mesh independence validation for SD-PHP at a heating power of 18 W and an FR of 50%.

Mesh numbers	4275	16,200	36,450	64,800
Thermal resistance (K/W)	1.563	1.747	1.795	1.802

The following parts compare the experimental data from Saha et al. [35] with the present numerical simulations to evaluate the model's correctness and dependability. The simulations replicated the geometric parameters and boundary conditions from Saha et al.'s experiment [35]. The condenser portion was kept at a constant temperature of 298.15 K (25 °C). At the same time, the evaporator part received constant heating inputs. Figure 4a presents a comparison between the experimental data and the numerical findings regarding the thermal resistance of the PHPs, defined as the ratio of the temperature differential between the evaporator and condenser sections (T_{evp}–T_{con}) to the applied heating power (Q). Figure 4a illustrates that the mean relative error in thermal resistance between the calculations and the testing is 5.04%. The peak error of 12.86% occurs with a heating input power of 45 W. Thus, the current numerical model effectively predicts the heat transfer in single-loop PHPs, particularly at low heat inputs, which was the primary focus of this study.

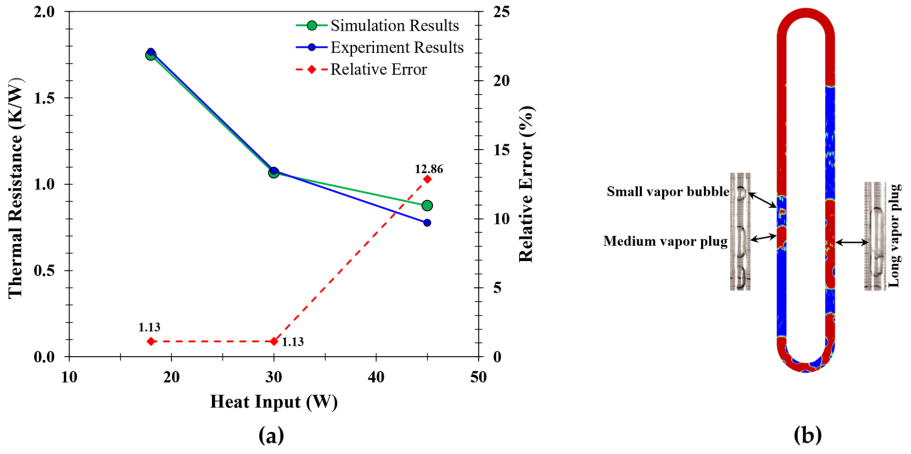


Figure 4. Comparison between the experimental findings of Saha et al. [35] and the current simulation outcomes for the SD-PHP: (**a**) thermal resistance at a heating power of 18, 30, and 45 W, and an FR of

50%, and (**b**) flow pattern at a heating power of 18 W and an FR of 40%. (reprinted from Ref. [35], Copyright 2024, with permission from Elsevier, Amsterdam, The Netherlands).

Moreover, the flow pattern observed in the numerical study was compared with that in the experimental study [35], as illustrated in Figure 4b. Both studies show good agreement, demonstrating a sequence of oscillation and circulation flows involving medium and long vapor plugs, with only a limited presence of small vapor bubbles.

3.2. Optimizing the Branch Diameter Difference

This section investigates the optimal branch diameter difference for the TD-PHPs under a low heating input power (18 W). A heat load of 18 W was selected to investigate the performance of four TD-PHP configurations—TD-PHP1, TD-PHP2, TD-PHP3, and TD-PHP4—because it is the only low heat input value (<25 W) for which experimental data for single-loop PHPs are available. The abovementioned configurations have the same wide branch and upper arch inner diameters (4 mm and 4.5 mm, respectively) but differ in the narrow branch inner diameters, ranging from 3.5 mm to 2 mm in decrements of 0.5 mm.

Figure 5 presents the thermal resistance values for these TD-PHPs. As the inner diameter of the narrow branch decreases, thereby increasing the branch diameter differences, a reduction in the thermal resistance is observed, from 1.55 K/W for the TD-PHP1 to 1.40 K/W for TD-PHP3. However, a further reduction in the narrow branch's inner diameter to 2 mm (in the TD-PHP4) results in a significant increase in thermal resistance, reaching 1.77 K/W. These findings indicate an optimal branch diameter difference with TD-PHP3, which features wide and narrow inner diameters of 4 mm and 2.5 mm, respectively.

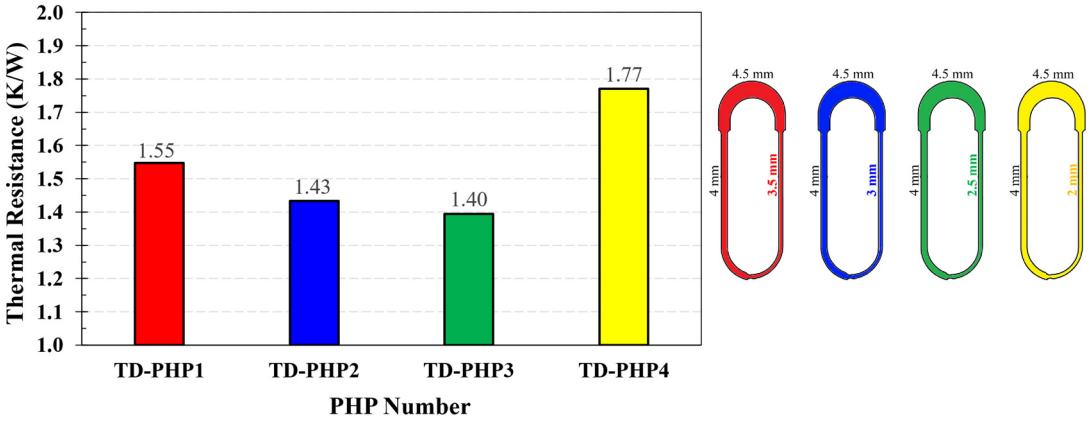


Figure 5. Thermal resistance of the TD-PHPs with various branch diameter differences.

Herein, the flow patterns within the TD-PHPs are examined to elucidate the mechanisms affecting their thermal performance, as the working fluid flow patterns heavily influence thermal efficiency. Generally, two basic flow modes—oscillation and circulation—are identified for these TD-PHPs. However, different TD-PHP configurations exhibit particular combinations and limitations of these two modes, which consequently lead to three distinct flow patterns: oscillation–circulation alternation (OC), full circulation (FC), and limited circulation (LC). Each flow pattern will be discussed in detail to provide additional clarification. Table 4 summarizes the flow patterns identified for the TD-PHP mentioned above.

Table 4. Flow patterns in TD-PHPs based on their configuration.

TD-PHP configuration	TD-PHP1	TD-PHP2	TD-PHP3	TD-PHP4
Flow pattern	OC	OC	FC	LC

In the circulation flow patterns, the working fluid moves from its initial branch to the second branch through the bottom and upper arches. This circulation can either complete an entire cycle, known as the FC flow pattern, or remain incomplete, referred to as the LC flow pattern.

Figure 6 displays a typical contour of the vapor volume fraction associated with the FC flow pattern for TD-PHP3. Notably, the FC flow pattern, unique to TD-PHP3, accelerates sensible heat transfer between the evaporator and condenser sections, resulting in the lowest thermal resistance [33].

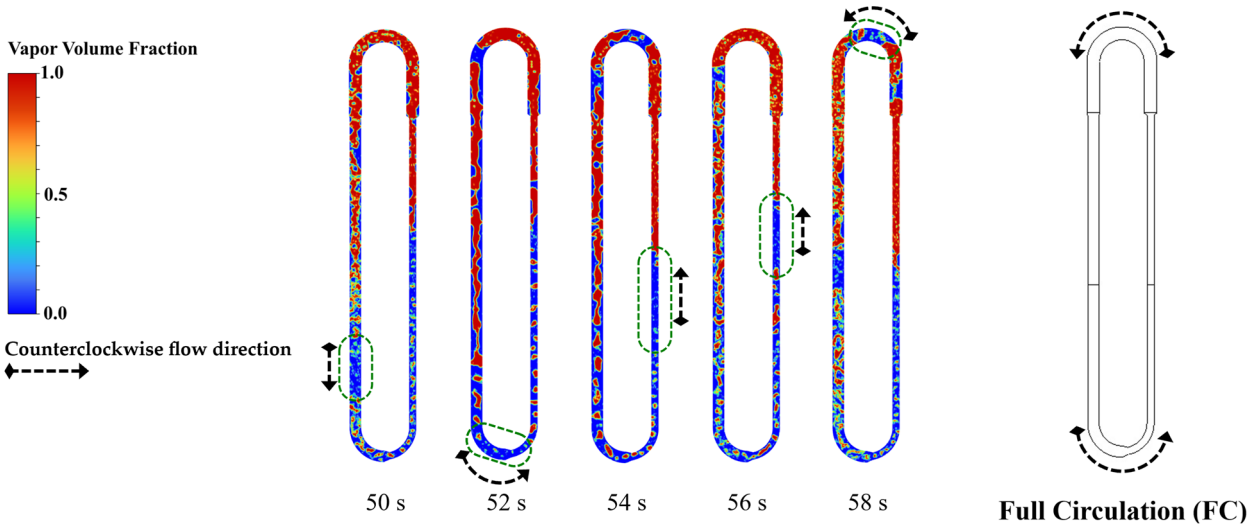


Figure 6. The full circulation (FC) flow pattern for TD-PHP3.

Interestingly, in the FC flow pattern for TD-PHP3, the movement of the working fluid occurs in a counterclockwise direction, as illustrated in Figure 6. At the start of the PHP's operation, the heating input power induces a liquid–vapor phase transition in the evaporator section, which includes portions of both the wide and narrow branches. As shown in Figure 7a, the narrow branch experiences a higher phase transition rate than the wide branch (see the boxes with red dashed lines) due to its lower liquid mass per unit of surface area. As depicted in Figure 7b, the increased vapor formation in the narrow branch results in higher dynamic pressure in the narrow branch (indicated by the box with dashed lines) and consequently moves the fluid towards the upper arch. This movement causes the working fluid to flow counterclockwise (Figure 7c,d). Additionally, the capillary pressure difference facilitates the movement of liquid from the wide branch to the narrow branch through the bottom arch (see Figure 7d), further promoting the counterclockwise flow circulation.

Liu et al. [33] reported a similar flow direction for DD-PHPs, while other studies (see, for example, Refs. [21,30]) showed a clockwise flow direction. The results of this investigation demonstrate that the swift initial phase change from liquid to vapor in the narrow branch considerably influences the flow direction. In both the current study and that of Liu et al. [33], a substantial portion of the PHP branches (40%) constitutes the evaporator section's main part, resulting in a rapid liquid–vapor phase transition and a counterclockwise flow direction. In contrast, the research by Kwon and Kim [30], in which only 15% of the branch length constituted the evaporator section, indicates that bubble formation at the bottom arch results in a clockwise flow direction (for further details, please refer to Ref. [30]).

Figure 5 illustrates that TD-PHP4 exhibits the LC flow pattern (see Table 3) and has the highest thermal resistance. The LC flow pattern is characterized by restricted fluid circulation. Figure 8 visually depicts the vapor volume fraction associated with the LC flow pattern, providing further insights into its behavior. In the LC flow pattern, the working

fluid initially moves from the narrow branch to the wide branch through the upper arch for reasons similar to those previously described. However, unlike the FC flow pattern, the LC pattern does not allow the fluid to freely return from the wide branch to the narrow branch through the bottom arch. This results in the liquid level in the wide branch remaining almost stable, with only limited oscillations.

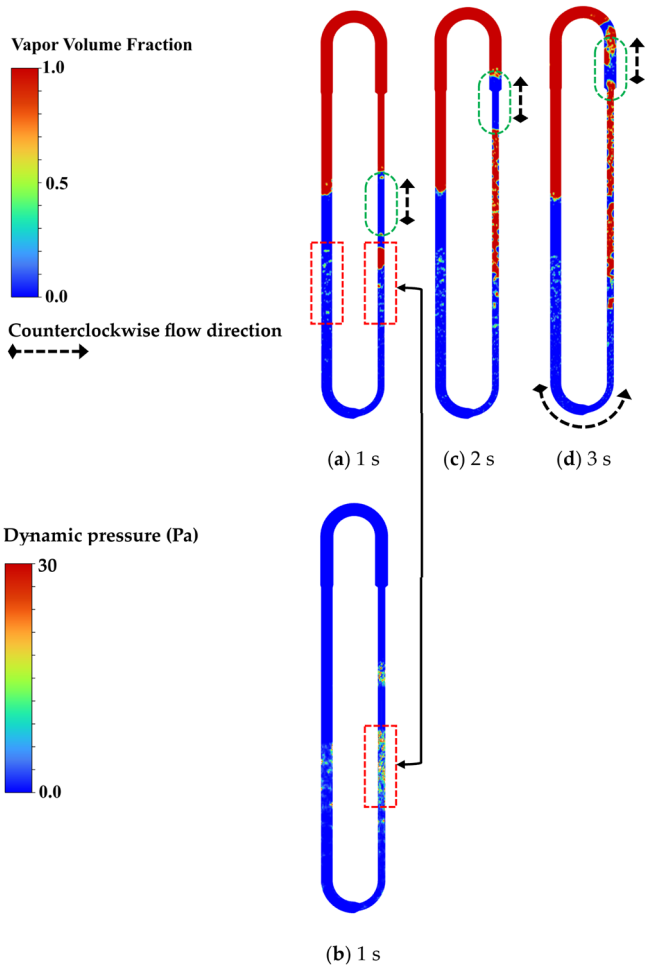


Figure 7. The dynamic pressure and vapor volume fractions for TD-PHP3 at the start of the operation.

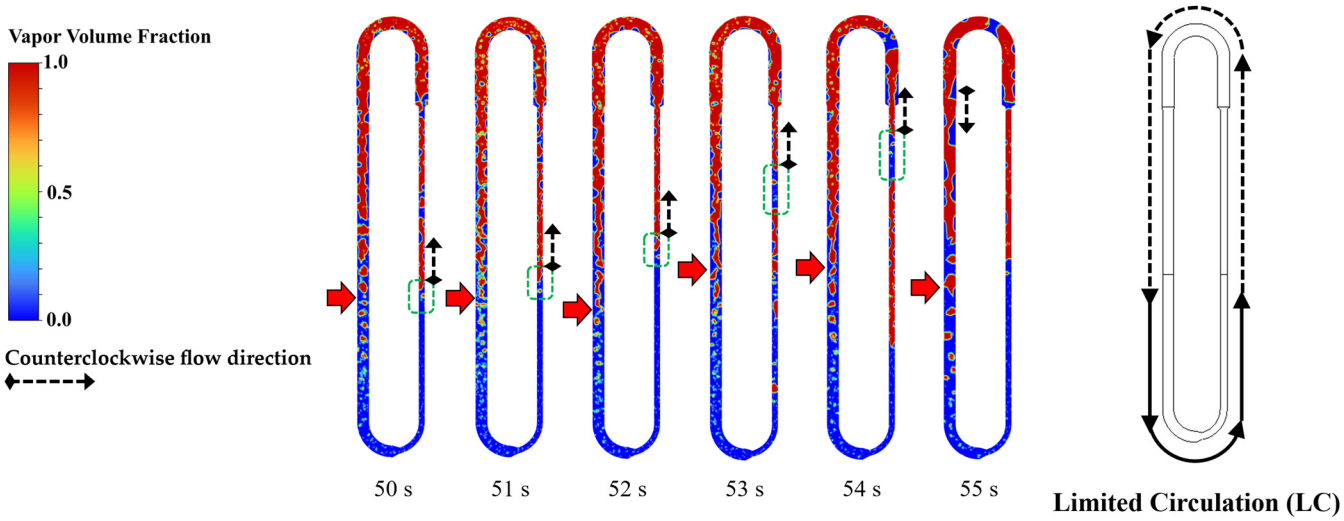


Figure 8. The limited circulation (LC) flow pattern for TD-PHP4.

This constraint is mostly attributable to the narrow channel's decreased inner diameter, which significantly exacerbates the influence of surface tension. As the inner diameter of the narrow channel approaches a value near the minimum critical of 1.908 mm, as calculated in Section 2.1, the surface tension exerts greater resistance against the fluid flow. This increased resistance hinders the fluid's free movement through the narrow channel, thereby preventing the completion of the full circulation flow. Consequently, TD-PHP4 shows significantly less sensible heat transfer, increasing the thermal resistance.

In conclusion, the analysis of the simulation results for TD-PHP3 and TD-PHP4 has demonstrated that a reduction in the inner diameter of the narrow branch results in the FC flow pattern with minimal thermal resistance. Conversely, TD-PHP1's and TD-PHP2's simulation results indicate that augmenting the inner diameter of the narrow branch diminishes the branch diameter disparities, subsequently reducing the capillary pressure at the bottom arch. This, in turn, partially disrupts the FC flow pattern, thereby leading to elevated thermal resistances. The disruption of the FC flow pattern occurs with the emergence of the oscillation mode (as typically illustrated in Figure 9). Interestingly, the emergence of the oscillation mode can also alter the flow direction for the following circulation mode. As a result, the OC flow pattern consists of a sequence of periodic emergences of the oscillation and arbitrary circulation flow modes.

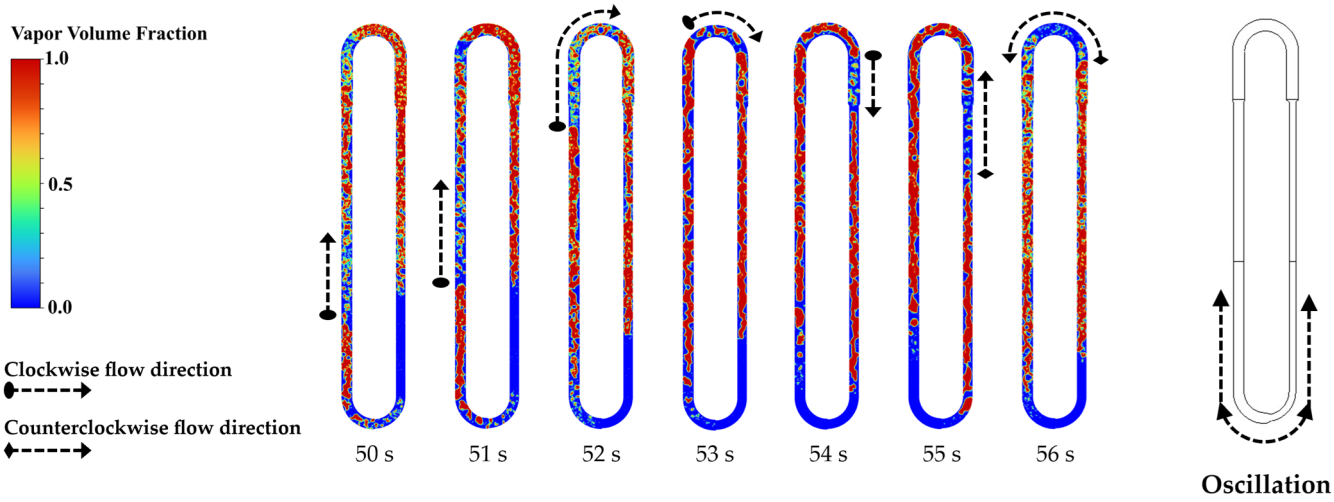


Figure 9. The oscillation flow mode for TD-PHP1.

3.3. Optimizing the Upper Arch Diameter

In the previous section, TD-PHP3 demonstrated the minimum thermal resistance with inner diameters of 2.5 mm for the narrow branch and 4 mm for the wide branch. This section compares the thermal efficiency of TD-PHP3, which has an upper arch inner diameter of 4.5 mm, with another TD-PHP configuration, TD-PHP5. TD-PHP5 shares the same narrow and wide branch diameters as TD-PHP3 but has a different upper arch inner diameter of 5 mm. Figure 10 provides a comparison of their thermal resistance. As observed, TD-PHP5, which features a larger upper arch diameter, exhibits a slightly higher thermal resistance compared with TD-PHP3. However, this difference is not significant.

It is worth noting that TD-PHP5 exhibits the OC flow pattern, unlike TD-PHP3, which displays the FC flow pattern. As previously mentioned, the enhancement of thermal performance is greater with the FC flow pattern compared with the OC flow pattern, making the lower thermal performance of TD-PHP5 justifiable.

As indicated in Section 3.2, increasing the inner diameter of the narrow branch reduces the branch diameter differences, which, in turn, decreases the capillary pressure at the bottom arch, partially disrupting the FC flow pattern. However, the simulation results presented here show that increasing the inner diameter of the upper arch beyond a critical value, approaching the maximum critical ID calculated in Section 2.1 (5.007 mm) can also

disrupt the FC flow pattern, albeit for a different reason, which is discussed in the following paragraph.

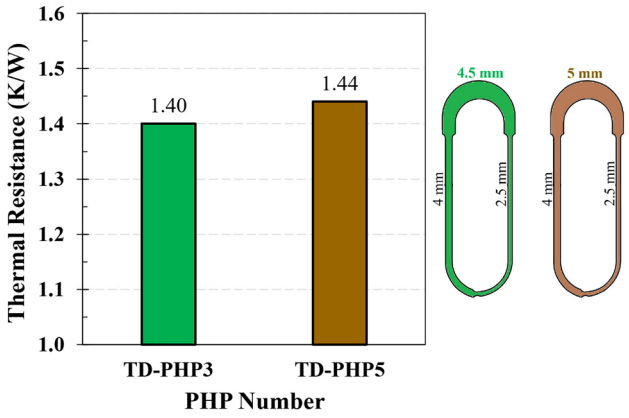


Figure 10. Thermal resistance of the TD-PHPs with various upper arch diameters.

The liquid slug at the junction between the narrow branch and the upper arch (see the dashed-line boxes in Figure 11) tends to move downward due to gravitational force. The capillary force arising from the difference in the inner diameters between the narrow branch and the upper arch further enhances this downward motion. In TD-PHP5, this difference in diameters is more pronounced than in TD-PHP3, resulting in a stronger capillary force acting on the fluid. Consequently, as depicted in Figure 11a, when the vapor plug from the narrow branch enters the upper arch (the condenser section) and partially condenses, as shown in Figure 11b,c, the formed liquid slug is unable to continue its counterclockwise movement, and the combined effects of gravitational and capillary forces keep the slug nearly stationary. Additionally, the condensed fluid from the upper part adds to the slug's mass (Figure 11d), further intensifying the gravitational force on the liquid slug. Eventually, these combined forces cause the slug to fall in a clockwise direction (Figure 11d), altering the working fluid's overall circulation direction within TD-PHP5.

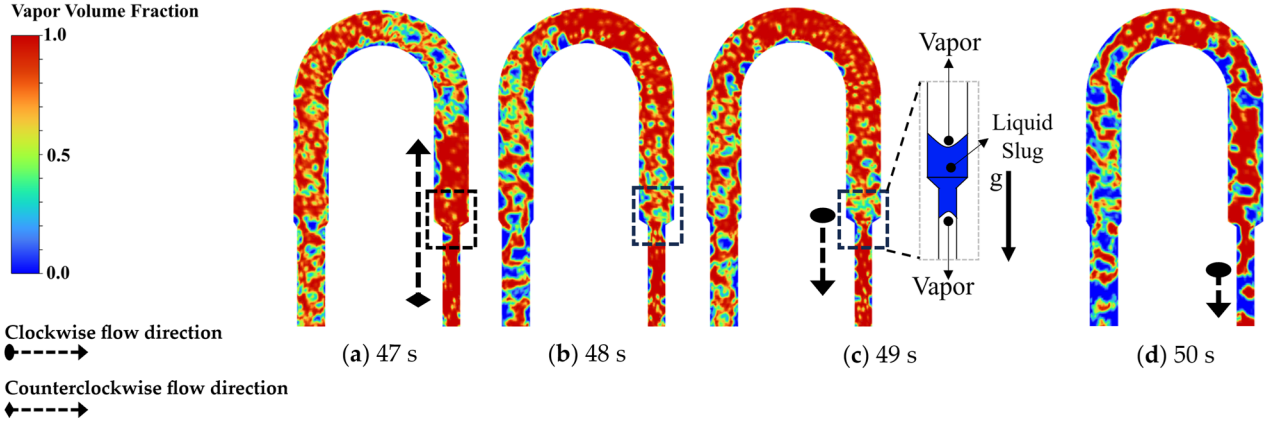


Figure 11. The liquid slug's behavior at the narrow branch and upper arch connection point for TD-PHP5.

3.4. Evaluating Low Heat Input Performance: TD-PHP3 Versus SD-PHP

This section compares the thermal performance of the optimal TD-PHP configuration, TD-PHP3, with the SD-PHP at low heating input powers of 10 W and 18 W. Due to the potential for stationary or oscillatory flow regimes in SD-PHPs at heat input powers below 10 W [30], a minimum heat input of 10 W was selected. This ensured that a circulation flow

mode was established for both SD-PHPs and TD-PHPs, enabling a direct comparison with the same flow regime.

In this analysis, thermal resistance values, as well as the start-up time, were examined to provide a comprehensive understanding.

As shown in Figure 12, TD-PHP3 demonstrates lower overall thermal resistance than the SD-PHP. This performance difference is attributed to the fact that TD-PHP3 exhibits the FC flow pattern at both 10 W and 18 W, while the SD-PHP exhibits the OC flow pattern, which is less efficient.

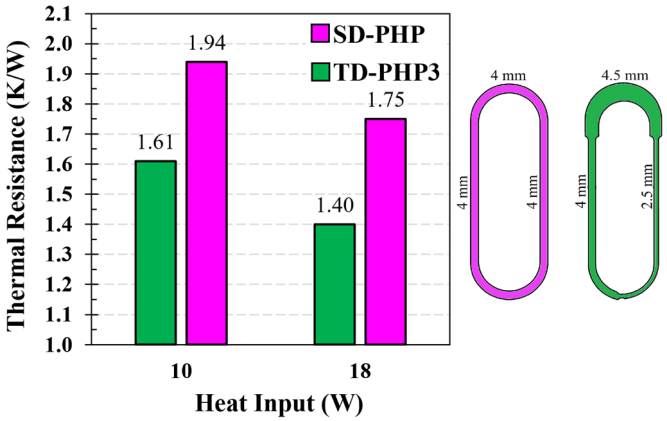


Figure 12. Thermal resistance of the SD-PHP and TD-PHP3 with a low heat input.

The results also show that reducing the heat input from 18 W to 10 W increases the thermal resistance for both TD-PHP3 and the SD-PHP. This increase in thermal resistance is due to the decreased velocity of the working fluid, a phenomenon that has been well-documented in the literature (see Ref. [25], for example). Figure 13 shows that the velocity of the working fluid in TD-PHP3 is notably higher under an 18 W heat input compared with a 10 W input. This higher fluid velocity at 18 W supports the explanation that increased working fluid speed enhances heat transfer efficiency, thereby reducing thermal resistance.

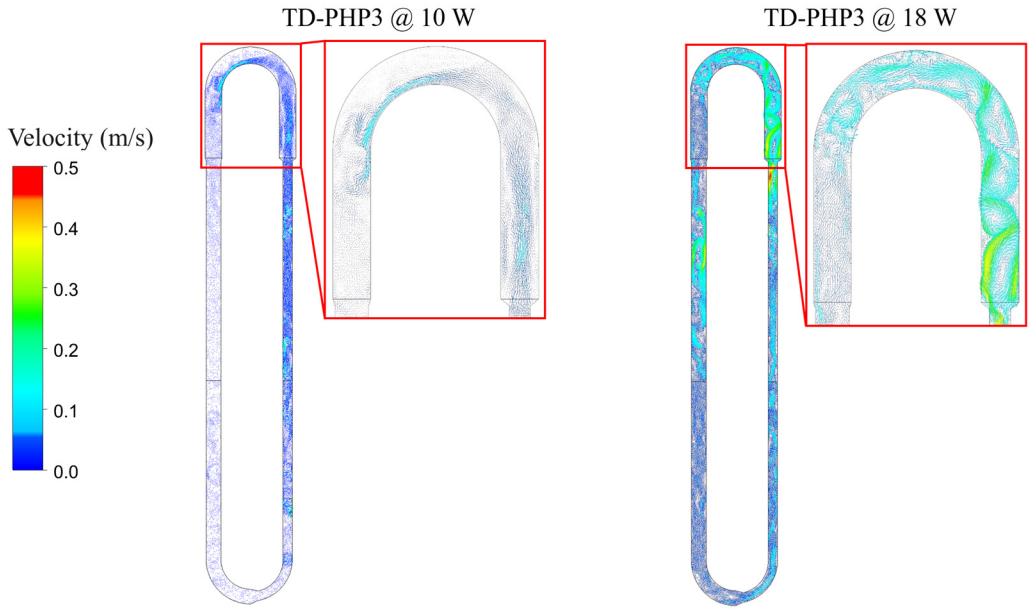


Figure 13. The effect of heat input variation on the working fluid through TD-PHP3.

More importantly, it should be noted that although TD-PHP3 exhibits lower thermal resistance compared with the SD-PHP at low heat inputs, it does not eliminate the adverse impact of reduced heating power on the performance of single-loop PHPs.

The start-up time is vital for understanding how PHPs respond to the heating input power. The use of heating power results in a consistent rise in the temperature of the evaporator wall, devoid of significant changes, indicating that the working fluid is efficiently absorbing energy. The energy build-up progressively amplifies the pressure differential between the evaporation and condensation phases. A considerable pressure differential propels the working fluid from the condensation section to the evaporation section, leading to a swift and marked reduction in the evaporator's temperature. This drop clearly indicates the PHP's successful start-up, signifying the onset of fluid movement and heat transfer within the system. An increase in the heating input power is anticipated to result in a more rapid elevation of the evaporator's temperature, an acceleration of the evaporation rate, and a more expeditious transition from the liquid to the vapor phase. These modifications typically result in a reduction in the time required for start-up. Nevertheless, as depicted in Figure 14, the augmentation of the heating power from 10 W to 18 W is relatively modest, resulting in an insignificant change in the start-up time.

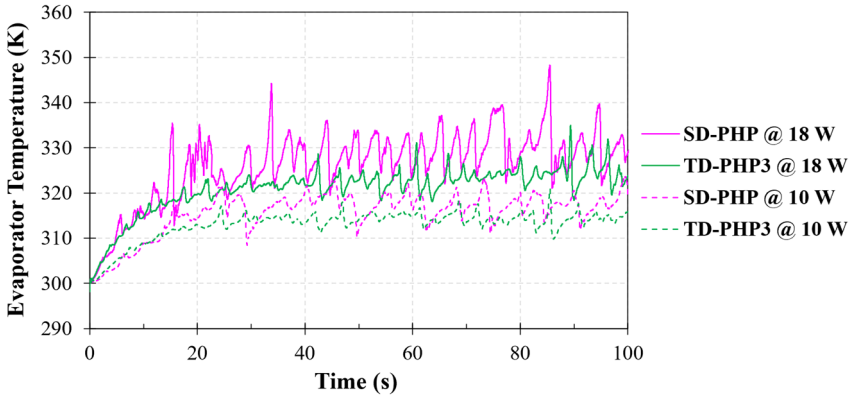


Figure 14. Variation in the evaporator's temperature with time for the SD-PHP and TD-PHP3 at 10 and 18 W of heat input.

Moreover, according to Fallahzadeh et al. [32], the TD-PHPs exhibit shorter start-up times compared with the SD-PHPs when subjected to medium heating input power levels (25–75 W). While the present simulation results demonstrate that at lower heating inputs of 10 W and 18 W, the disparity in start-up times between the TD-PHP3 and SD-PHP configurations is not significant, it is noteworthy that all configurations exhibit a start-up time of approximately 20 s.

4. Conclusions

By using computational fluid dynamics simulations, this study determined the optimal inner diameters for single-loop triple-diameter pulsating heat pipes (TD-PHPs) under low heating input powers. This process included analyzing the thermal performance, particularly the thermal resistance, and examining the flow patterns in various TD-PHP configurations with differing inner diameters. Additionally, the thermal performance, including the thermal resistance, start-up time, and start-up temperature, of the optimally designed TD-PHP was compared with that of a single-loop single-diameter pulsating heat pipe (SD-PHP). In the simulated single-loop PHPs, three distinct flow patterns are observed: oscillation–circulation alternation (OC), full circulation (FC), and limited circulation (LC). The flow patterns significantly influence the thermal performance of PHPs. The findings may be encapsulated as follows.

1. The difference in inner diameters between the wide and narrow branches significantly affects the thermal resistance of TD-PHPs. As the branch diameter difference

increases, thermal resistance decreases and then increases. Optimal thermal resistance is achieved with wide and narrow diameters of 4 mm and 2.5 mm, respectively, corresponding to the FC flow pattern.
2. TD-PHPs with a branch diameter difference smaller than the optimal value exhibit the OC flow pattern, while those with a branch diameter difference larger than the optimal value display the LC flow pattern.
3. The thermal resistance of TD-PHPs is less sensitive to variations in the inner diameter of the upper arch (the condenser section) compared with the diameters of the wide and narrow branches. However, when the inner diameter of the upper arch increases to 5 mm, the potential to disrupt the FC flow pattern rises, resulting in higher thermal resistance.
4. Compared with the SD-PHP, the optimal TD-PHP exhibits lower thermal resistance while maintaining nearly the same start-up time.

Nevertheless, it is important to note that the thermal performance of PHPs is influenced by a variety of factors that can significantly alter both the flow regime and thermal resistance. These parameters include, but are not limited to, the thermal and physical properties of the working fluid, the specific conditions of microgravity or hypergravity under which the PHP operates, the degree of surface roughness in the channel walls, the FR of the working fluid, the evaporator–condenser length ratio, and the inclination angle. Given the complexity and interplay of these variables, there is a pressing need for further research to thoroughly analyze and understand how each of these factors impacts the performance of the optimal TD-PHP that has been developed.

Additionally, because a two-dimensional CFD simulation was conducted in the present study, it is essential for future research to perform a comparative assessment to evaluate the outcomes derived from both two-dimensional and three-dimensional CFD models.

Author Contributions: Writing—original draft preparation, R.F., M.H.G. and L.P.; writing—review and editing, R.F. and L.C.; software, R.F., M.H.G. and L.P.; supervision, F.B. and L.C. All authors have read and agreed to the published version of the manuscript.

Funding: The work was funded under the National Recovery and Resilience Plan (NRRP) Mission 4 Component 2 Investment 1.5—Call for tender No. 3277 of 30/12/2021 of Italian Ministry of University and Research funded by the European Union – NextGenerationEU (Award Number: Project code ECS00000033, Concession Decree No. 1052 of 23/06/2022 adopted by the Italian Ministry of, CUP D93C22000460001, "Ecosystem for Sustainable Transition in Emilia-Romagna" (Ecosister)).

Data Availability Statement: The original contributions presented in the study are included in the article, further inquiries can be directed to the corresponding authors.

Conflicts of Interest: The authors declare no conflicts of interest.

References

1. Wang, Q.; Tao, J.; Cui, Z.; Zhang, T.; Chen, G. Passive enhanced heat transfer, hotspot management and temperature uniformity enhancement of electronic devices by micro heat sinks: A review. *Int. J. Heat Fluid Flow* **2024**, *107*, 109368. [CrossRef]
2. Li, Z.; Luo, H.; Jiang, Y.; Liu, H.; Xu, L.; Cao, K.; Wu, H.; Gao, P.; Liu, H. Comprehensive review and future prospects on chip-scale thermal management: Core of data center's thermal management. *Appl. Therm. Eng.* **2024**, *251*, 123612. [CrossRef]
3. Mousa, M.H.; Yang, C.M.; Nawaz, K.; Miljkovic, N. Review of heat transfer enhancement techniques in two-phase flows for highly efficient and sustainable cooling. *Renew. Sustain. Energy Rev.* **2022**, *155*, 111896. [CrossRef]
4. Akachi, H. Structure of a Heat Pipe. U.S. Patent 4921041, 5 May 1990. [CrossRef]
5. Jouhara, H.; Chauhan, A.; Nannou, T.; Almahmoud, S.; Delpech, B.; Wrobel, L.C. Heat pipe based systems—Advances and applications. *Energy* **2017**, *128*, 729–754. [CrossRef]
6. Xu, Y.; Xue, Y.; Qi, H.; Cai, W. An updated review on working fluids, operation mechanisms, and applications of pulsating heat pipes. *Renew. Sustain. Energy Rev.* **2021**, *144*, 110995. [CrossRef]
7. Nikolayev, V.S.; Marengo, M. Pulsating Heat Pipes: Basics of Functioning and Modeling. In *Encyclopedia of Two-Phase Heat Transfer and Flow IV*; Nolan, D.P., Ed.; World Scientific Publishing: Singapore, 2024; pp. 63–139. [CrossRef]
8. Mu, H.; Shi, W. Review of Operation Performance and Application Status of Pulsating Heat Pipe. *Sustainability* **2024**, *16*, 2722. [CrossRef]

9. Fazli, M.; Mehrjardi, S.A.A.; Mahmoudi, A.; Khademi, A.; Amini, M. Advancements in pulsating heat pipes: Exploring channel geometry and characteristics for enhanced thermal performance. *Int. J. Thermofluids* **2024**, *22*, 100644. [CrossRef]
10. Lee, J.; Joo, Y.; Kim, S.J. Effects of the number of turns and the inclination angle on the operating limit of micro pulsating heat pipes. *Int. J. Heat Mass Transf.* **2018**, *124*, 1172–1180. [CrossRef]
11. Charoensawan, P.; Terdtoon, P. Thermal performance of horizontal closed-loop oscillating heat pipes. *Appl. Therm. Eng.* **2008**, *28*, 460–466. [CrossRef]
12. Nikolayev, V.S. Physical principles and state-of-the-art of modeling of the pulsating heat pipe: A review. *Appl. Therm. Eng.* **2021**, *195*, 117111. [CrossRef]
13. Pagliarini, L.; Iwata, N.; Bozzoli, F. Pulsating heat pipes: Critical review on different experimental techniques. *Exp. Therm. Fluid Sci.* **2023**, *148*, 110980. [CrossRef]
14. Kim, B.; Li, L.; Kim, J.; Kim, D. A study on thermal performance of parallel connected pulsating heat pipe. *Appl. Therm. Eng.* **2017**, *126*, 1063–1068. [CrossRef]
15. Sedighi, E.; Amarloo, A.; Shafii, M.B. Experimental investigation of the thermal characteristics of single-turn pulsating heat pipes with an extra branch. *Int. J. Therm. Sci.* **2018**, *134*, 258–268. [CrossRef]
16. Kommur, S.; Reddy, N.M.; Basumatary, K.K.B.; Venugopal, S. Numerical study on single turn pulsating heat pipe with additional branch configuration. *Heat Transf. Eng.* **2023**, 1–17. [CrossRef]
17. Kang, Z.; Shou, D.; Fan, J. Numerical study of a novel single-loop pulsating heat pipe with separating walls within the flow channel. *Appl. Therm. Eng.* **2021**, *196*, 117246. [CrossRef]
18. Liu, S.; Li, J.; Dong, X.; Chen, H. Experimental study of flow patterns and improved configurations for pulsating heat pipes. *J. Therm. Sci.* **2007**, *16*, 56–62. [CrossRef]
19. Chien, K.H.; Lin, Y.T.; Chen, Y.R.; Yang, K.S.; Wang, C.C. A novel design of pulsating heat pipe with fewer turns applicable to all orientations. *Int. J. Heat Mass Transf.* **2012**, *55*, 5722–5728. [CrossRef]
20. Chiang, C.M.; Chien, K.H.; Chen, H.M.; Wang, C.C. Theoretical study of oscillatory phenomena in a horizontal closed-loop pulsating heat pipe with asymmetrical arrayed minichannel. *Int. Commun. Heat Mass Transf.* **2012**, *39*, 923–930. [CrossRef]
21. Kwon, G.H.; Kim, S.J. Experimental investigation on the thermal performance of a micro pulsating heat pipe with a dual-diameter channel. *Int. J. Heat Mass Transf.* **2015**, *89*, 817–828. [CrossRef]
22. Yang, K.S.; Cheng, Y.C.; Liu, M.C.; Shyu, J.C. Micro pulsating heat pipes with alternate microchannel widths. *Appl. Therm. Eng.* **2015**, *83*, 131–138. [CrossRef]
23. Jang, D.S.; Lee, J.S.; Ahn, J.H.; Kim, D.; Kim, Y. Flow patterns and heat transfer characteristics of flat plate pulsating heat pipes with various asymmetric and aspect ratios of the channels. *Appl. Therm. Eng.* **2017**, *114*, 211–220. [CrossRef]
24. Aref, L.; Fallahzadeh, R.; Shabanian, S.R.; Hosseinzadeh, M. A novel dual-diameter closed-loop pulsating heat pipe for a flat plate solar collector. *Energy* **2021**, *230*, 120751. [CrossRef]
25. Markal, B.; Varol, R. Experimental investigation and force analysis of flat-plate type pulsating heat pipes having ternary mixtures. *Int. Commun. Heat Mass Transf.* **2021**, *121*, 105084. [CrossRef]
26. Markal, B.; Candere, A.C.; Avci, M.; Aydin, O. Effect of double cross sectional ratio on performance characteristics of pulsating heat pipes. *Int. Commun. Heat Mass Transf.* **2021**, *127*, 105583. [CrossRef]
27. Markal, B.; Candere, A.; Avci, M.; Aydin, O. Investigation of flat plate type pulsating heat pipes via flow visualization-assisted experiments: Effect of cross sectional ratio. *Int. Commun. Heat Mass Transf.* **2021**, *125*, 105289. [CrossRef]
28. Yu, J.; Hong, S.; Koudai, S.; Dang, C.; Wang, S. An experimental investigation on the heat transfer characteristics of pulsating heat pipe with adaptive structured channels. *Energies* **2023**, *16*, 6988. [CrossRef]
29. Kwon, G.H.; Kim, S.J. Study on the flow and heat transfer characteristics of pulsating heat pipe with asymmetric configuration. In Proceedings of the International Technical Conference and Exhibition on Packaging and Integration of Electronic and Photonic Microsystems, Burlingame, CA, USA, 16–18 July 2013.
30. Kwon, G.H.; Kim, S.J. Operational characteristics of pulsating heat pipes with a dual-diameter tube. *Int. J. Heat Mass Transf.* **2014**, *75*, 184–195. [CrossRef]
31. Wang, J.; Pan, Y.; Liu, X. Investigation on start-up and thermal performance of the single-loop pulsating heat pipe with variable diameter. *Int. J. Heat Mass Transf.* **2021**, *180*, 121811. [CrossRef]
32. Fallahzadeh, R.; Aref, L.; Bozzoli, F.; Cattani, L.; Gholami, H. A novel triple-diameter pulsating heat pipe: Flow regimes and heat transfer performance. *Therm. Sci. Eng. Prog.* **2023**, *42*, 101902. [CrossRef]
33. Liu, Y.; Dan, D.; Wei, M.; Zheng, S.; Sun, J. Numerical investigation on the start-up and heat transfer performance of dual-diameter pulsating heat pipes. *Appl. Therm. Eng.* **2024**, *236*, 121709. [CrossRef]
34. Wang, C.; Yuan, K.; Song, Q.; Yu, J.; Yang, J.; Qu, J.; Zhu, Y. Performance of pulsating heat pipe with a stimulus of auxiliary heat load for battery thermal management systems. *Int. J. Heat Mass Transf.* **2024**, *223*, 125190. [CrossRef]
35. Saha, N.; Das, P.K.; Sharma, P.K. Influence of process variables on the hydrodynamics and performance of a single loop pulsating heat pipe. *Int. J. Heat Mass Transf.* **2014**, *74*, 238–250. [CrossRef]
36. Khedher, N.B.; Togun, H.; Abed, A.M.; Al-Najjar, H.M.; Dulaimi, A.; Mohammed, H.I.; Mahdi, J.M.; Yvaz, A.; Talebizadehsardari, P. Discharge performance assessment of a vertical double-pipe latent heat storage unit equipped with circular Y-shaped fins. *J. Build. Eng.* **2023**, *75*, 106870. [CrossRef]

37. Anto, L.P.; Varghese, J. Three-dimensional steady state numerical analysis of inclined two phase closed thermosyphon for solar applications. *Case Stud. Therm. Eng.* **2022**, *30*, 101805. [CrossRef]
38. Lee, W.H.; Lyczkowski, R.W. The basic character of five two-phase flow model equation sets. *Int. J. Numer. Methods Fluids* **2000**, *33*, 1075–1098. [CrossRef]
39. Wu, H.L.; Peng, X.F.; Ye, P.; Gong, Y.E. Simulation of refrigerant flow boiling in serpentine tubes. *Int. J. Heat Mass Transf.* **2007**, *50*, 1186–1195. [CrossRef]
40. Brackbill, J.U.; Kothe, D.B.; Zemach, C. A continuum method for modeling surface tension. *J. Comput. Phys.* **1992**, *100*, 335–354. [CrossRef]
41. Henderson-Sellers, B. A new formula for latent heat of vaporization of water as a function of temperature. *Q. J. R. Meteorol. Soc.* **1984**, *110*, 1186–1190. [CrossRef]
42. Chen, T.; Liu, S.; Shen, Y.; Gao, B.; Mazhar, A.R. A novel triangular pulsating heat pipe with enhanced heat transfer performance for building energy efficiency. *Case Stud. Therm. Eng.* **2023**, *49*, 103286. [CrossRef]

Disclaimer/Publisher's Note: The statements, opinions and data contained in all publications are solely those of the individual author(s) and contributor(s) and not of MDPI and/or the editor(s). MDPI and/or the editor(s) disclaim responsibility for any injury to people or property resulting from any ideas, methods, instructions or products referred to in the content.